Version of Record: https://www.sciencedirect.com/science/article/pii/S2214860420305558
Manuscript_4057224e1bfd82188012a32cfe2b8ebf

Unraveling Pore Evolution in Post-Processing of Binder Jetting Materials: X-Ray Computed Tomography, Computer Vision, and Machine Learning

Yunhui Zhu [a,*], Ziling Wu [a], W. Douglas Hartley [b], Jennifer M. Sietins [c], Christopher B. Williams [d], Hang Z. Yu [b, †]

[a] Bradley Department of Electrical and Computer Engineering, Virginia Tech, Blacksburg, VA 24061, USA

[b] Department of Materials Science and Engineering, Virginia Tech, Blacksburg, VA 24061, USA

[c] CCDC Army Research Laboratory, Aberdeen, MD 21005, USA

[d] Department of Mechanical Engineering, Virginia Tech, Blacksburg, VA 24061, USA

**corresponding author: yunhuiz@vt.edu*
[†] corresponding author: hangyu@vt.edu

Quality control in metal additive manufacturing prioritizes the development of advanced inspection schemes to characterize the defect evolution during processing and post-processing. This involves grand challenges in detecting internal defects and analyzing large and complex defect datasets in macroscopic samples. Here, we present an inspection pipeline that integrates (i) fast, micro X-ray computed tomography reconstruction, (ii) automated 3D morphology analysis, and (iii) machine learning-based big data analysis. X-ray computed tomography and automated computer vision result in a holistic defect morphology database for the inspected macroscopic volume, based on which machine learning analysis is employed to reveal quantitative insights into the global evolution of defect characteristics beyond qualitative human observation. We demonstrate this pipeline by examining the global-scale pore evolution in post-processing of binder jetting additive manufacturing, from the green state, to the sintered state, and to the hot isostatic pressed state of copper. The pipeline is shown to be effective at detecting and processing the information associated with a large number (~10^5) of pores in macroscopic volumes. The subsequent principal component analysis and clustering analysis extract the key morphological descriptors and categorize the detected pores into four morphological groups. By quantifying the evolution of (i) the weight of pore morphology parameters and (ii) the pore number and volume fraction of each categorized group, new understandings are developed regarding the effects of sintering and hot isostatic pressing on pore decomposition, shrinkage, and smoothing during post-processing of binder jetting.

Keywords: binder jetting; pore analysis; X-ray computed tomography; computer vision; machine learning

1. Introduction

Recent years have witnessed the rapid development of various metal additive manufacturing (AM) technologies, from powder bed fusion, directed energy deposition, and binder jetting, to additive friction stir deposition, allowing for net-shaping of a broad range of metals and alloys [1-9]. However, AM also features a variety of defects like pores, internal micro-cracks, and air bubbles that can be present in massive quantities with heterogeneous distributions in the as-printed materials [5, 10], and is found to severely degrade the static and fatigue mechanical properties and thus the reliability of the binder jetting parts [11]. The reliability of AM parts critically depends on our quality control capabilities, which allows optimization and thereby allows reducing or eliminating these defects [12]. This necessitates the development of advanced inspection schemes to enable complete volumetric examination on the macroscopic level as well as comprehensive understandings of the defect characteristics and their global evolution during AM and post-processing.

Understanding defect evolution has been challenging in current AM research [13-15]. The first challenge comes from the acquisition of the defect information throughout macroscopic volumes. A lot of work in AM has focused on local defect characterization using destructive approaches, in which a slice of material is subjected to optical, scanning electron, or transmission electron microscopy [16-18]. These approaches are valid only if the defect information of the slice is representative of the whole material, which is rarely the case for metal AM—the printed material has location-dependent thermal histories that are governed by the component geometries and hatch patterns. In contrast, ultrasonic wave or X-ray allows for non-destructive testing of large volumes; as a result, tools like pulse-echo ultrasonic testing, laser ultrasonic testing, and X-ray computed tomography (XCT) are becoming popular in metal AM inspection [19-22]. Among them, XCT stands out for its superior spatial resolution and deep penetration capability that can provide rich 3D morphological information for all internal defects [21-23]. For example, inspections of porosity in Laser Powder Bed Fusion based additive manufacturing has been widely explored with X-ray CT scan, revealing a rich database of porosity emerged from various mechanisms, such as keyhole collapse [24] and lack of fusion [25]. However, the porosity in LPBF systems has significantly

different spatial distribution and morphological properties from the pores in binder jetted materials; the LPBF pores are usually much less densely populated and often clustered, while binder jetting is characterized by large numbers of pores that are universally distributed in the sample [10, 11]. New analyzing approaches are needed to efficiently address the challenges associated with binder jetted materials. In addition, high-resolution XCT for large-scale sample is slow; it may take hours to characterize a millimeter-scale volume with micrometer-scale spatial resolution.

The second challenge stems from automated defect registration. While the high-resolution volumetric XCT data provides comprehensive structural information, the size of the dataset is massive (~ 2-15 GB), involving a large quantity of 3D defects with morphological features spanning over several orders of magnitude. As a result, defect identification and characterization need to be automated with 3D morphological analysis algorithms. Some commercial software codes, such as FEI Avizo [26], and free image analysis software, such as ImageJ/Fiji [27, 28], are able to perform the semi-automated defect analysis for XCT data to provide some useful information of defects, such as porosity fraction, pore area/volume size, position, etc. in 2D slices [27] or 3D volume [26]. These pre-defined parameters, however, are not optimal to characterize the pores morphological features in binder jetted samples, such as extrusion and necking. This limits the capability for quantitative defect categorization and dynamic evolution analysis. More comprehensive and reliable morphological characterization approaches tailored for the binder jetting are needed. Recently, there has been great interest in developing computer vision based automated inspection [14, 29-31]; in particular, deep learning approaches have enabled example-based rather than conventional rule-based algorithms [32, 33]. Progress in this regard will facilitate automated 3D analysis approaches for advanced inspection in metal AM.

The third challenge lies in efficient data analysis of defects with complex shapes, where quantification of the morphology is essential to understand the global defect evolution during AM and post-processing. Currently, the defect information in AM is typically represented by a single metric, porosity, which is the volume fraction of pores [34-36]. The porosity can effectively describe the quality of AM parts *only if* the spatial distribution of pores is uniform and all of the pores are similar in sizes and shapes. It is also well known that porosity alone is insufficient to account for the part properties such as permeability, elastic anisotropy and fracture toughness [37, 38], which are highly dependent on the pore shape, orientation, and spatial distribution. Understanding the underlying correlations and trends for large defect datasets is therefore of

paramount importance. Such quantification and assessment can be explored through statistical extremes, such as the maximum volume [39, 40]. Here, we explore an alternative big data approach to extract evolutional features from the comprehensive dataset of all pores.

Quantitative big data analysis not only provides a holistic picture for global defect evolution during AM or post-processing, but can also give rise to new physical insights beyond vision-based qualitative description [41].

To address all these challenges, the goal of this work is to establish a new inspection approach for AM research in binder jetting materials, which integrates the recent advances in (i) fast tomography, (ii) 3D morphological analysis, and (iii) machine learning-based big data analysis. Leveraging deep learning algorithms, fast tomography is used to collect high-resolution XCT data with only a fraction of the normal data acquisition time [42-45]. Employment of computer vision algorithms allows us to process large sets of X-ray CT data for holistic defect registration and morphology parameterization more reliably and efficiently. The big data analysis enables us to extract the key morphological descriptors of the defects and to categorize the defects into multiple morphological groups based on feature similarity [46-50]. As a result, global defect evolution during AM or post-processing can be quantified, and the most salient changes of defect characteristics can be revealed.

Here, we demonstrate this method by examining the post-processing in binder jetting additive manufacturing, which involves substantial global pore evolution from the green state, to the sintered state, and to the hot isostatic pressed (HIPed) state. We use copper as a model system, which is difficult to print using powder bed fusion and directed energy deposition due to the high reflectivity and high thermal conductivity [51], but are readily printed by binder jetting with good quality—as long as the internal pores can be effectively reduced via post-processing. We show that the approach is effective at detecting and handling the information associated with the large number (~10^5) of pores in macroscopic samples, and the pore morphology can be sufficiently represented by a few morphological descriptors based on principal component analysis (PCA). The detected pores are found to be best categorized into four morphological groups, including quasi-spherical pores, small elongated pores with high solidity (a.k.a. convexity, which is used to quantify the amount of concavities of a shape within in its convex boundary. See Supplementary Figure 2 for more information regarding the definition of solidity.), large elongated pores with low

solidity, and reticulated defects. By quantifying the evolution of the pore morphological parameters and the weight of each categorized morphological group, we find a reduction in the pore size and eccentricity after sintering and HIP. During sintering, the interconnected reticulated defects break up into smaller pores, while the HIP process is more effective at reducing the size and increasing the solidity of the isolated pores.

2. The Inspection Pipeline of Defect Evolution in Metal Binder Jetting AM

The proposed pipeline consists of three modules: (i) fast micro X-ray computed tomography, which enables quick collection of 3D defect data in a macroscopic volume using sparse-view tomography techniques; (ii) automated 3D morphological analysis, based on which the collected data is processed for defect registration and morphology parameterization; (iii) principal component analysis and clustering analysis, by which key morphological descriptors of the defects are extracted and the defect morphology evolution is quantified during post-processing. Fig. 1 depicts a flowchart for the three modules and their connections.

2.1. Micro X-ray computed tomography (μXCT)

Global-scale AM characterization necessitates efficient and accurate acquisition of the 3D morphological data of defects. A tomographic scan is performed to acquire projection images of the object from different viewing angles. In this work, full view construction is first performed in μXCT characterization of the binder jetted samples. To reduce the data acquisition time, we also explore fast tomography, in which a convolutional neural networks (CNN)-based reconstruction algorithm will be used to enhance the imaging quality from sparse-view CT.

Traditional reconstruction algorithms, such as filtered back-propagation (FBP), suffer from severe reconstruction artifacts like streak effect and blurring [52-54]. Using deep learning approaches, a network is trained to learn the prior features of the object as well as the reconstruction artifacts. The training sample data consists of paired datasets of under-sampled reconstructions and the corresponding high-fidelity ground truth from idealized acquisition conditions. The trained network is used for imaging translation [43, 55-58], in which new under-sampled reconstructions are converted into high-fidelity estimates. For the binder jetted copper samples in this work, we use a hierarchical synthesis CNN (HSCNN) to improve the sparse-view CT reconstruction. This is implemented through image translation, where under-sampled reconstructions are converted into high-fidelity estimates via trained neural networks [45].

HSCNN involves a hierarchical split-and-combine architecture, as illustrated in Fig.1. The networks first split the training data into three different resolutions to train three CNNs separately. These feature maps on the three length-scales are then combined in a second training stage to yield the final high-fidelity reconstruction. (See supplementary information for full architecture parameters.) The capability of feature recognition across different spatial resolutions in HSCNN has proven to be beneficial in characterizing 3D cellular and architectured materials [59, 60].

2.2. Automated 3D morphological analysis for pore morphology parameterization

To register the defects and parametrize their 3D morphology, the raw voxel-based 3D data from μXCT (~2 GB) need to be processed using computer vision algorithms. First, the voxel brightness distribution is sorted and fit to an expectation function of a bimodal Poisson model [53], where the mean brightness of the expectation function is set to be consistent with the density of the measured sample. This step removes unevenness from background illumination. Second, an adaptive segmentation algorithm is implemented to differentiate low-density regions (pore or binder domains) from high-density regions (metal) [52, 55]. This step binarizes the gray-scale images to reduce the data size by three orders of magnitude (from 2 GB to 400 MB). Last, each potential pore region is identified from the 3D binary data using connectivity analysis, and the target regions are extracted and cross referenced with the gray-scale dataset. If the potential pore is well padded (i.e., surrounded by a gradual transition region), it will be considered as a true pore and will be registered. Otherwise, it will be considered as an artifact and ignored. The output of this step is a full list of registered pores, which will be stored as connected voxel clusters.

The registered 3D pores are then parametrized to form a morphology data pool $\boldsymbol{F}$. For each pore, we first register the volume v based on the number of voxels and then register the surface area s by fitting the pore surface with triangular meshes [61]. The pore shape and orientation are determined based on ellipsoidal representation. Such geometrical approximation allows us to register the principal axis length (a, b, and c), the axis orientation (θ and φ), the centroid location (x_o, y_o, and z_o), and the bounding box size (x, y, and z) of each pore. Finally, we characterize the pore solidity using convex hull. The convex hull of a closed region is the smallest convex set that contains the region (see Supplementary Figure 2 for more information). The volume of each convex hull is recorded as v_{hull}. The corresponding solidity can be measured by the ratio between the actual volume and convex hull volume: v/v_{hull}, which ranges from 0 to 1. Solidity effectively

characterizes the pore shapes in terms of convexity, which quantifies ratio of concavities of a shape in comparison to its convex bounding hull volume. High solidity means the volume is more convex and low solidity means there are more concave boundaries. For a spherical pore, the actual volume is the same as the convex hull volume and the solidity is 1. For a pore resulting from a network of multiple narrow particle gaps, the convex hull volume is much larger than the actual volume, and the solidity is much smaller than 1. The pore morphology is registered with the variables summarized in Table 1. The holistic morphology data allows for statistical analysis of pore size, eccentricity, and orientation distributions.

Table 1. Registered pore morphology variables.

Elliptical representation				Voxel counting & Mesh fitting		Convex hull
Centroid coordinates	Orientation	Principal axis lengths	Bounding box size	Volume	Surface area	Volume
$\boldsymbol{x_o\ y_o\ z_o}$	$\theta\ \phi$	$a\ b\ c$	$x\ y\ z$	v	s	v_{hull}

2.3. Principal component analysis and clustering analysis

Morphology parameterization of all pores in the entire specimen allows for objective feature selection without sampling bias using big-data analytical tools. In this module, we aim to find the key descriptors that most efficiently represent the morphology variations among the pores, and characterize the pore evolution within the key descriptor domain. We utilize the principal component analysis (PCA) [49] to remove the redundancy from correlations between the analyzed dataset (e.g., partial correlation between the volume and surface area).

Formally speaking, given the N morphology parameters for M pores, we register the $N \times M$ matrix $\boldsymbol{F} = \{f_{ij}, i = 1, \dots N, j = 1, \dots M\}$ to establish a pore morphological feature library. The PCA method generates the uncorrelated orthogonal basis set $\boldsymbol{P} = \{P_i, i = 1, \dots N\}$—the principal components, where each P_i is a linear combination of the N feature variables in $\boldsymbol{F}$. These principal components (PCs) are ordered by their component variance (starting from the most important P_1 to the least important P_N). Selecting the first few P_is allows for the optimal preservation of the morphology differences with a reduced representation. The reduced PC domain provides a natural basis to describe the morphology evolution of pores.

Finally, we categorize the pores into different morphological groups by identifying clusters that are maximally separated in the reduced PC domain. This is achieved through the Gaussian mixture model (GMM) clustering [46, 50], which fits the dataset into multi-variate normal components that maximize the component posterior probability. The optimization algorithm involves iteratively updating cluster centroid, covariance matrices, and mixing proportion, and assigning data points to the clusters with the maximum expectation [61]. As compared to other clustering methods such as k-means [48], GMM clustering provides a universal framework that allows us to compare different clustering numbers and covariance structures. Two information criteria are employed, Akaike information criterion (AIC) and Bayesian information criterion (BIC) [62, 63], to evaluate the effectiveness and accuracy of the clustering models. Both AIC and BIC estimate the relative amount of information lost from a fitting model: less information loss indicates a higher quality for the model, which is represented by lower values of AIC and BIC. These two techniques penalize a large number of clusters to prevent overfitting. Here we employ the minimization of AIC and BIC to choose an adequate clustering model that represents the dataset without exceeding complexity. This analysis enables quantification of the major trend of global defect evolution based on objective, data-driven approaches.

3. Experimental Procedures

3.1. Material

Copper samples were additively manufactured using binder jetting, followed by several post-processing steps. The copper powder used in this study was spherically shaped featuring a bimodal diameter distribution with peaks at 5 µm and 30 µm. The two types of powders were mixed in the ratio of 27:73 by weight using a low energy ball mill for ~ 2 hours.

3.2. Specimen manufacturing

Binder jetting additive manufacturing was conducted using an ExOne R2 3D printer at a layer thickness of 70 µm. Standard binder PM-B-SR2-05 provided by ExOne was used at a 100% binder saturation value. More details of the AM parameters were elaborated elsewhere [64, 65].

The green copper sample consisted of two phases: loosely packed copper particles and numerous binder domains [66, 67]. The first step in post-processing was de-binding, which was carried out at 450 °C (53% melting temperature of copper) for 0.5 hour in a reducing hydrogen

environment. The second step was sintering, which was carried at 1075 °C (99% melting temperature of copper) for 3 hours in the same environment. The third step was hot isostatic pressing (HIP), which was carried out at 1075 °C under an argon pressure of 206.84 MPa for 2 hours. Three experiments were performed under the same binder jetting conditions but were stopped at different steps of post-processing. Experiment 1 involved no post-processing; Experiment 2 involved de-binding and sintering; Experiment 3 involved de-binding, sintering, and HIP. The three corresponding samples were labeled as 'green', 'sintered' and 'HIPed' respectively. All these three samples imaged through X-ray tomography are cut into 3.8 x 3.8 x 3.8 mm^3 to fit into the field of view.

3.3. Micro X-ray computed tomography

For each copper sample, the 3D defect morphology was scanned using a laboratory-based micron-scale X-ray tomography platform (ZEISS Xradia Versa 520, Carl Zeiss X-ray Microscopy Inc., Pleasanton, CA) with a voxel size of 3.7× 3.7 × 3.7 μm^3 and a total volume of 1024 × 1024 × 1024 voxels. This was equivalent to a macroscopic volume of 3.8 × 3.8 × 3.8 mm^3. The field of view covered the entire volume of the samples, which were cut into 2×2×2 mm^3 cubes and placed close to the source. Tomographic scan was implemented with the voltage of 160 KeV and the current of 200 μA. In the full-view configuration, 3201 projections were performed for high-quality reconstruction, which took around four hours. For sparse-view tomography, only 201 projection images were scanned for each sample with the same operating parameters. The sparse-view scan took around 15 minutes, approximately 16 times of reduction compared to full-view experiment. The raw transmission projection images were reconstructed using a commercial image reconstruction software package (ZEISS XMReconstructor, Carl Zeiss X-ray Microscopy Inc., Pleasanton, CA) which employed a filtered back-projection algorithm. For sparse-view reconstruction, the HSCNN algorithm was performed to improve reconstruction quality. We cropped 1740 patches with the size of 256×256 pixels randomly from the first 100 sparse-view reconstructed images and the corresponding full-view reconstructed images as the network datasets; 80% were used for training, and the rest were used for testing. The training of the network was implemented using MATLAB 2018b (Mathworks, Natick, MA, USA). The trained network was then used to enhance the rest, untrained slices by translating each patch in the new slice into the enhanced output. These output patches were stitched accordingly to retrieve the reconstruction

result. The processor was Intel Core i7-6700K, the memory was 32 GB, and the GPU was one NIVIDIA GeForce GTX 960 card. In this configuration environment, it took about 6 hours to train samples over the network for one type of data. Once trained, it took only around 4 seconds for the translation of one full slice.

All the post-processing, including the Automated 3D morphological analysis for pore morphology parameterization, Principal component analysis, and clustering analysis, were performed using MATLAB 2018b (Mathworks, Natick, MA, USA).

4. Results and Discussion

4.1. µXCT reconstruction

The µXCT reconstruction results are shown in Fig. 2 and Fig. 3 as 2D slices and 3D volumetric renderings for the green, sintered, and HIPed samples. It should be noted that the pores are filled with binder in the green sample but are not in the sintered and HIPed samples. For convenience, in all the cases we use 'pore' to refer to the space that is not filled by copper, regardless of whether it is filled by the binder.

The morphology evolution of the pores can be identified from the reduction of porosity and pore sizes. In the green state, there are numerous pores, which are generally elongated, irregularly shaped, and in some cases highly interconnected. Quantitative analysis confirms that the percentage of such reticulated defects makes up over 90% of the relative pore volume fraction. After burn-out of the binders and sintering, the part has significantly increased its density, and network-like interconnected pores are seen to break up into a large number of more isolated pores (from 22, 912 in green sample to 54, 739 in sintered sample). After the final post-processing stage (HIP), many small pores disappear, leading to reduction in the total number of pores from the sintered sample (40,018 in HIPed sample). The mean pore size keeps decreasing during this process (from 20, 322 μm^3 in the green sample to 14, 593 μm^3 in the sintered sample, and to 4, 842 μm^3 in the HIPed sample). A change of the pore shape is also observed—the pores become more spherical, which is reflected in the increase of solidity (from 0.6532 in green to 0.6840 in sintered sample, and to 0.7026 in the HIPed sample). Overall, after each post-processing step, it is evident that the pores become smaller in size, and the smaller pores are generally more spherical in shape.

The effectiveness of the fast X-ray CT algorithm is demonstrated for the green sample. Fig. 4 shows a comparison between (1) the sparse-view reconstruction (based on 201 projections), (2) the full-view reconstruction (based on 3201 projections), and (3) the corresponding enhancement using the hierarchical synthesis CNN algorithms discussed in Section 2.1. Clearly, the blurring and streak artifacts shown in the sparse-view reconstruction have been effectively removed. Validation on a number of slices also proves that the pore registration results from the enhanced sparse-view reconstruction (i.e., the 3rd column) are very close to that from the full-view reconstruction (i.e., the 2nd column). We employed two parameters, mean square error (MSE) and structure similarity index (SSIM), to quantitatively assess the reconstruction results from the developed HSCNN algorithm. The MSE between the sparse-view reconstruction result (Fig. 4a) and the ground truth reconstructed from full-view CT (Fig. 4b) is 0.0073. Using the HSCNN algorithm, this error is reduced to 0.0030 (Fig. 4c), while the SSIM increases from 0.5439 to 0.7407. We also compared the 2D porosity fraction and pore size results based on extracted pores of these three slices (Fig. 4d-f). While the total porosity of the three slices is obtained as 33.08%, 33.52% and 33.44% for sparse-view using the traditional FBP algorithm, full-view reconstruction (ground truth), and sparse-view reconstruction using the HSCNN algorithm, respectively. While the measured porosity is similar, the distribution of pore sizes is more accurately captured with HSCNN than that with the traditional FBP algorithm. There are 320 pores in the sparse-view reconstruction result (Fig. 4d), 112 pores (ground truth) in the full-view reconstruction (Fig. 4e), and 115 pores in the sparse-view reconstruction with HSCNN algorithm (Fig. 4f). The mean pore area of these three slices are 931 μm^2, 2696 μm^2(ground truth), 2619 μm^2, respectively. These quantitative comparisons show the reliability and efficiency of HSCNN algorithm for sparse-view CT reconstruction. With reduction in the number of projection measurement by a factor of 16, we have been able to obtain the high-resolution CT scan within 15 minutes, as compared to 4 hours of data acquisition in full-view reconstruction.

While the developed fast tomography method for enhanced sparse-view reconstruction works well for the green sample, the performance is less impressive for the sintered and HIPed samples. The spherical shape of the as-printed particles provides a strong prior structural feature for the fast tomography reconstruction for the green sample, but this feature becomes substantially weaker after sintering and HIP as individual particles are merged through surface diffusion. In the

following analysis, therefore, the fast tomography approach is used for the green sample, whereas the full-view tomography approach is used for the sintered and HIPed samples.

4.2. Morphological and statistical analysis results

Table 2: Registered pore morphology data

Pore Index	Centroid µm			Orientation °		PA length µm			Bounding box size µm			Volume µm³	Surface area µm²	Convex hull volume µm³
	x_o	y_o	z_o	θ	ϕ	a	b	c	x	y	z	v	s	v_{hull}
1	5.3	48.1	2.2	57.6	95.2	51.4	17.4	13.2	44.4	22.2	14.8	3.19e3	1.55e3	7.70e3
2	2.5	273	5.7	33.8	120.5	39.3	25.9	14.4	29.6	25.9	44.4	6.13e3	2.23e3	1.02e4
3	27.9	80.9	14.3	72.2	74.7	283	112	89.4	241	189	163	2.14e5	5.37e4	2.31e6
4	13.0	412	39.0	54.5	264.2	254	127	54.8	137	122	244	2.50e5	5.69e4	1.64e6
5	4.9	295	6.3	78.2	9.6	24.5	33.4	21.2	33.3	59.2	40.7	1.27e4	4.21e3	3.34e4
:		:			:		:					:	:	:
117669	61	40	600	90	251.6	23.5	8.2	4.3	18.5	11.1	3.7	455.90	302.8	557.2

The collected X-ray imaging data of copper samples is processed to yield a total pore number of 117,669, including 22,912 pores in the green sample, 54,739 in the sintered sample, and 40,018 in the HIPed sample. Pore morphology is parameterized for all pores using the approach elaborated in Section 2.2, with a small portion of the parameterization results shown in Table 2. Based on the pore morphology database, a statistical analysis is implemented. The porosity of the green, sintered, and HIPed sample is measured as 37.90%, 3.43%, and 0.89%, respectively. We measured the density of the samples via the conventional Archimedes method [64] for the sintered and HIPed samples, and obtained 95.5% and 99.2% of density, respectively. These measurements are consistent with results from the 3D pore analysis. Fig. 5 (a) shows the evolution of pore size distribution, which consistently shifts to the smaller side (left) from the green sample to the sintered and to the HIPed sample. Notably, the green sample features a singular, massive interconnected void that is shown as a single bar on the far right in the histogram plot. Originating from the pore network interconnected throughout the entire sample, the giant defect accounts for 35% of the total pore volume. After sintering, this massive singular defect breaks up into a large number of smaller pores. We will use the machine learning analysis to further quantify pore decomposition to identify correlated morphology changes in addition to the volume reduction (Section 4.3).

Fig. 5 (b) plots the distribution of pore number density (calculated as the number of pores per 1×10^{-3} mm^3) based on cumulative probability to evaluate the randomness of spatial distribution

for the pores. For randomly distributed pores, the volumetric density distribution should follow Poisson's distribution $P(\lambda) = e^{\lambda}\frac{\lambda^k}{k!}$, where k is the number density. When comparing the detected pore number density (dotted lines) to the Poisson's distribution (dashed lines), the sintered and HIPed samples demonstrate good fitting, indicating that pore size distribution in these two samples is approximately random. The density distribution of the green sample significantly deviates from the Poisson's distribution, which is likely due to the influence by the printing trajectory. Fig. 5 (c) plots the evolution of pore eccentricity, e_l, which is defined as the ratio of the longest principal axis to the equivalent radius. Going from the green to the sintered, and to the HIPed sample, a left-ward shift of the curve is observed, indicating *less* eccentric, or *more* spherical, pore shapes after post-processing.

Fig. 6 plots and compares the pore orientation distribution of the three samples. The orientation of each pore is defined as the direction along the longest axis of the ellipsoid. As shown in Fig. 6 (a), the 3D orientation is represented by the altitude angle θ (the angle of the orientation vector with respect to the vertical axis or the build direction) and the azimuth angle ϕ (the angle of projected orientation vector on the horizontal plane with respect to the reference of x axis). A small altitude angle θ close to 0° indicates that the pore is vertically orientated, while $\theta \sim 90°$ represents a pore that is flat on the horizontal plane. While the green sample contains a primary interconnected pore that takes up 35% of the porosity volume, the remaining 65% of porosity is made up of 22,911 separated pores with well-defined orientations. In Fig. 6, we plot the orientation distribution based on pore number.

The registered data of the altitude angle and azimuth angle is statistically analyzed. Fig. 6 (b) compares the distribution of the altitude angle θ among samples at different post-processing stages. In the green sample, the altitude angle appears to distribute randomly between 90° (i.e., within the print layers) and 0° (vertical to the print layers), without obvious orientation preference. However, in both sintered and HIPed samples, it is observed that the pore orientation is more closely aligned with the printing plane, as evident by the distribution peaks at 90°. The apparent difference of the pore orientation between the green and the post-processed samples may stem from the particle rearrangement during sintering, in which more particles fall down and shrink the pores along the vertical direction. Note that there is no evidence of gravity playing a role in the large-scale heterogeneity of the pore distributions in the sample. Instead, it is only observed locally that

particles tend to fall closer vertically than move closer horizontally under the influence of gravity. This gravity-influenced particle rearrangement has been observed in similar granular systems as well and is likely to be responsible for the observed anisotropy of pore orientation after sintering [68]. As a result, the pores are more likely to be flattened out on the horizontal plane with larger altitude angles. The altitude anisotropy is not significantly altered after the HIP process, which can be attributed to the application of isotropic pressure.

Fig. 6 (c) displays the orientation distribution in polar plots, where the radial axis represents the altitude angle, and the circumferential axis represents the azimuth angle. For the sintered and HIPed samples, the polar plot shows concentration of data points near the edge, which is consistent with the altitude anisotropy observed in Fig. 6 (b). There are no azimuth orientation preferences in all samples, which suggests that the printing trajectory direction does not impose a preferred in-plane orientation to the pores.

4.3. Quantitative pore evolution analysis using machine learning

4.3.1. Principal component analysis

The first step in analyzing global defect evolution is to extract the key morphological descriptors for the pores. These key morphological descriptors enable quantitative representation of the pore morphology with reduced dimensions. To implement the PCA analysis, the morphology data in Table 2 is re-scaled to yield a normalized dataset. This standard procedure improves the numerical stability and avoids the emphasis on certain variables with extreme values, and is commonly used [69]. The normalized morphology parameters are shown in Table 3.

The PCA analysis results are shown in Fig. 7. It can be seen that the combination of volume and eccentricity is of primary importance to PC1 and PC2, which account for 55% and 24% of the explained variance respectively. Interestingly, PC3 (12% of the explained variance) almost entirely consists of the altitude angle. This indicates that the inclination angle is uncorrelated with other morphological features. Overall, decomposition into the first four PCs accounts for 97% of the explained variance, or morphology differences, of all the registered pores, whereas the generic principal components represent the morphological features of the pores that stay unchanged during the post-processing. For the purpose of pore evolution analysis, we focus on the leading PC to describe the most salient changes. The following analysis is based on the reduced 4-PC representation.

Table 3: Pore morphology parameter library

Index	Notation	Attribute	Normalization
1	v	Volume	$\widehat{\log v}$
2	e_l	Eccentricity 1	$a/\sqrt[3]{abc}$
3	e_m	Eccentricity 2	$b/\sqrt[3]{abc}$
4	e_s	Eccentricity 3	$c/\sqrt[3]{abc}$
5	η	Compactness	$\sqrt{S}/\sqrt[3]{v}$
6	r	Volume ratio	v/xyz
7	s	Solidity	v/v_{hull}
8	θ	Altitude angle	θ

4.3.2. Clustering analysis

After PCA, clustering analysis is implemented in the reduced 4-dimensional PC space using GMM clustering. To determine the optimal cluster number, such analysis has been performed for scenarios of various cluster numbers (with cluster number of 1 to 8). The clustering results are evaluated by two information criteria, AIC and BIC. It is found that the best classification with the smallest intra-cluster covariance is achieved at the cluster number of 4 as shown in Fig. S3 in the Supplementary information. In other words, the detected pores in all three binder jetted copper samples are best categorized into four morphological groups.

For visualization, the clustered data points are plotted in the 3D space spanned by PC1, PC2, and PC3 in Fig. 8 (a). For the subspace defined by each cluster, the data points at the center of the subspace represent the typical morphology of the corresponding pore group. Fig. 8 (b) shows the typical 3D pore morphology for each of the four groups, which can be interpreted as:

- Group 1: quasi-spherical pores. These pores are predominately classified by their small volume ($0.32 \pm 0.39 \times 10^4\ \mu m^3$), low eccentricity ($e_l: 1.51 \pm 0.21, e_m: 0.97 \pm 0.10, e_s: 0.70 \pm 0.09$), high solidity ($0.76 \pm 0.13$), high volume ratio ($0.35 \pm 0.13$), and absence of sharp edges or extrusions. Pores meeting these classification criteria are the most numerous in the detected samples.

- Group 2: small elongated pores (volume: $0.97 \pm 0.41 \times 10^4\ \mu m^3$) with high solidity ($0.51 \pm 0.13$). These pores are characterized by eccentric structures but without significant extrusions, which results in high solidity.
- Group 3: large elongated pores (volume: $3.61 \pm 0.52 \times 10^4\ \mu m^3$) with low solidity ($0.36 \pm 0.12$). These pores are usually elongated, displaying a lot of extrusions and necking that result in low solidity.
- Group 4: reticulated defects (volume: $5.56 \pm 1.58 \times 10^4\ \mu m^3$, solidity: 0.33 ± 0.12). Characterized by a tortuous, network topology, these defects are composed of large packing voids that are interconnected. The average volume of these defects is larger than that of any previous group.

4.3.3. Quantitative evolution of the pore morphology

We next use the clustering basis to quantify pore morphology evolution. Figs. 9 (a)-(c) show the clustering results for the green, sintered, and HIPed samples. Figs. 9 (d) and (e) present the quantitative evolution with respect to pore number fraction and relative pore volume fraction (given pore volume/total pore volume). In terms of pore number fraction, Group 1 pores are of the largest number in all stages (green, sintered, or HIPed), as shown in Fig. 9 (d). In terms of relative pore volume fraction, however, the weight of each pore group changes significantly during the post-processing stages, as shown in Fig. 9 (e). We observe a steady reduction of the reticulated defects (Group 4) throughout the post-processing stages. In the green sample, the reticulated defects make up over 90% of the relative pore volume fraction, despite being less than 10% of the pore number fraction. The relative pore volume fraction of the reticulated pores decreases to 42.3% after the sintering, and further decreases to 20.5% after HIP. The reduction of the reticulated pore is accompanied by the steady increase of the quasi-spherical pores (Group 1), from 4% relative volume fraction in the green sample to 25% in the sintered sample, and to 48% in the HIPed sample.

Overall, during post-processing of binder jetting the main source of porosity shifts from Group 4 (>90% relative pore volume fraction in the green sample) to Group 1 pores (48% relative pore volume fraction in the HIPed sample). On the other hand, the behavior of Group 2 and Group 3 pores is not characterized by a simple trend, involving an increase of number fraction and relative

volume fraction by the sintering process, and then a decrease of number fraction after the HIP process.

We have also explored the evolution of pore morphology by tracking the changes of morphological parameters (Table 3) within each category. We calculate the average of volume v, solidity s, compactness η, and the altitude angle θ within each category, and plot the results in Fig. 10. We observe a general trend that the morphology changes are more significant for the larger pores in Group 3 and 4, and less obvious for smaller pores in Group 1 and 2. For example, v and η of Group 3 and 4 pores have steadily decreased during both sintering and HIP, but these parameters stay almost the same for the smaller pores. The solidity of Group 3 and Group 4 pores increases during the post-processing from ~ 0.3 (green) to ~ 0.4 (HIPed). For Group 1 pores, the solidity almost stays the same at a high value of 0.75 during post-processing. We have also observed a significant increase of the altitude angle in all groups of pores after sintering, suggesting that all groups of pores become more aligned with the printing plane after sintering. Such orientation changes are particularly noteworthy for the small pores, i.e., Group 1 and Group 2 pores.

4.4. Discussion: physical insights from data analytics

The data analytical results in 4.3 provide quantitative physical insights into pore evolution during the post-processing of binder jetting. Initially, the binder infiltrates among the loosely packed particles, forming large and mostly interconnected gaps. The green sample is observed with a high porosity of 37.90%, which is predominately a result of these reticulated defects. The reticulated defects (Group 4) consist of tortuous, interconnected voids, and typically contain multiple narrow regions among particles in contact. During sintering, neighboring particles form neck structures at the contacting locations as a result of densification diffusion. The growth of the neck structure brings the particles closer together with overall pore shrinkage [70]. At the same time, neck growth of the particle contact can lead to breakup of the interconnected pores and future decomposition of large pores, resulting in more discontinuous pores that belong to Group 2 and Group 3. The pore shrinkage and pore breakup explain the increased number and average size of Group 2 and Group 3 pores after the sintering step, despite the overall shrinkage of pore sizes. It is also observed that the orientation of the pores favors the horizontal direction after sintering, indicating that a greater degree of shrinkage occurs along the vertical direction. This anisotropy is

considered to be a result of particle rearrangement under the influence of gravity during sintering. These findings are consistent with previous studies based on the 2D characterization of pores [5, 68, 71].

During the final stage of HIP, the pore morphology is observed to favor isolated and geometrically regular pore classifications (Groups 1 and 2). These results can be explained by the continuation of particle neck growth via surface diffusion, which is accelerated by the isostatic pressure during HIP. Intense, isotropic diffusion during HIP introduces future decomposition of large pores into small pores with high solidity. At the same time, it also smooths the pore shape and further reduces the pore size. As a result, the solidity continuously increases and eccentricity decreases during HIP, i.e., pores become steadily smoother and more isotropic. The orientation of the pores remains largely unchanged during the HIP process, suggesting that gravity is no longer influential in the presence of isostatic pressure from all directions. At the final stage of pore evolution, small quasi-spherical pores may shrink below the threshold of μXCT detection or completely close up, leading to the substantial reduction of pore number at the end the post-processing. These pore morphology evolution mechanisms are illustrated in Fig. 11.

As compared to previous inspection schemes for AM or post-processing, the presented approach shows several unique advantages. Firstly, we can efficiently extract the 3D pore morphology information based on fast 3D data acquisition. The sparse-view acquisition reduces the scanning time by a factor of 16, while parameterization of automated morphology registration takes only 10 min for around 105 pores on a single GPU desktop. The revealed 3D analysis results correctly record the reticulated or interconnected morphology of Group 4 pore, which would be segmented into isolated intersection areas using 2D projection characterization. This is why the analysis of Group 4 pores with the complex geometries and low solidity requires 3D characterization by CT. Secondly, the analyzing approach provides a holistic inspection for a large quantity of pores, whose morphological properties are described with a comprehensive set of parameters. As compared to current commercial defect analysis software codes, such as FEI Avizo[26], and ImageJ/Fiji [27, 28], where automated defect analysis can be implemented to yield a limited number of pore property parameters such as size and location[26,27], our approach provides a much more complete set of morphological parameters including pore orientation, surface area, principal lengths, sphericity, aspect ratio, etc. These parameters are more reliable and efficient to fully describe the static pore morphology and dynamic defect evolution involving

complex morphology features such as extrusion and necking. In addition, the machine learning approach identifies the most efficient pore morphology descriptor space with reduced dimensions, while current software can only implement analysis on pre-defined parameters according to general criteria. This approach allows us to categorize a large number of pores into different groups with the most salient morphological differences. Finally, the high-resolution 3D inspection reveals fine pores after the HIP process, albeit at a final relative density $> 99\%$. The information on these residual pores is valuable for studying the final stage of pore closure during consolidation in future material and manufacturing research.

The machine learning method provides a reliable approach to identifying and separating the varying parameters from the constant parameters, and thus enables the efficient representation of the most salient changes during the pore evolution. It has proven to be a powerful tool to remove redundancy in the input data. The success of the analysis, as a result, relies on a comprehensive input dataset that covers all relevant factors. For example, the presented analysis does not include the location information in the input dataset, because of the observed uniformity of pore distribution as illustrated in Fig. 6(a). If heterogeneity becomes important, descriptors such as height, distance to the surface, shall become necessary and should be included in the dataset.

5. Conclusions and Outlook

To summarize, we have presented a new inspection pipeline to characterize the defect evolution in post-processing of binder jetting. Through the integration of fast tomography, 3D morphology analysis and machine learning, we demonstrate a pathway toward efficient acquisition of holistic defect information and robust morphological representation. The key contributions of this work include:

- Hierarchical synthesis CNN (convolutional neural networks)-based fast tomography algorithms yield high-fidelity 3D tomography reconstruction of the defects in macroscopic volumes, using only a fraction of the typical acquisition time. This has been successfully demonstrated in the green binder jetted copper sample. Using automated computer vision involving 3D segmentation and connected region measurement, a total number of ~10^5 pores has been registered with their 3D morphological features parameterized to establish a comprehensive defect library.

- Using unsupervised machine learning (PCA and GMM clustering), the key morphological descriptors of the pores are extracted, and the detected pores are effectively categorized into four morphological groups with distinct features. This allows for quantification of the pore morphology evolution based on the established descriptors and clusters, which is beyond the capability of human vision due to the large size of datasets and the complex 3D pore geometries that span multiple length scales.
- The advanced 3D inspection and data analytics provide new physical insights into pore evolution during post-processing of binder jetting. It has been revealed that many of the reticulated pores (Group 4) in the green state break up into small (Group 2) and large elongated pores (Group 3) during sintering, leading to an increase of the volume fraction and number fraction of Group 2 and Group 3 pores. The most salient pore morphology change by HIP includes a significant increase of the volume fraction of the small quasi-spherical (Group 1) pores due to pressure-accelerated diffusion and overall smoothing of the pore shape, accompanied by an increase of solidity of Group 3 and Group 4 pores.

For future work, the presented inspection pipeline can be improved in several aspects. The framework can be validated with porosity data from other established methods, such as that in the work by Hermanek et al., with which the accuracy and traceability can be quantified [72]. The code used in this work is available online at https://github.com/Ziling-Wu/HSCNN_Matlab for data validation in other relevant scenarios. The resolution of the μXCT tomography can be improved to the sub-μm level, to include small pores and resolve sharp peaks at the boundary of the pores. More effective deep learning algorithms can be developed for fast tomography to reduce the data acquisition time. More advanced data analytical tools can be incorporated, e.g., to better represent the topology of network defects, and to include the potential interaction of adjacent pores.

Acknowledgement. Part of this work was performed under the Virginia Tech-ARL CRADA #16-13. YZ would like to acknowledge the National Science Foundation (grant number QMR-1825646) for partial support. The authors would like to thank Mackenzie E.J. Perry for helpful comments.

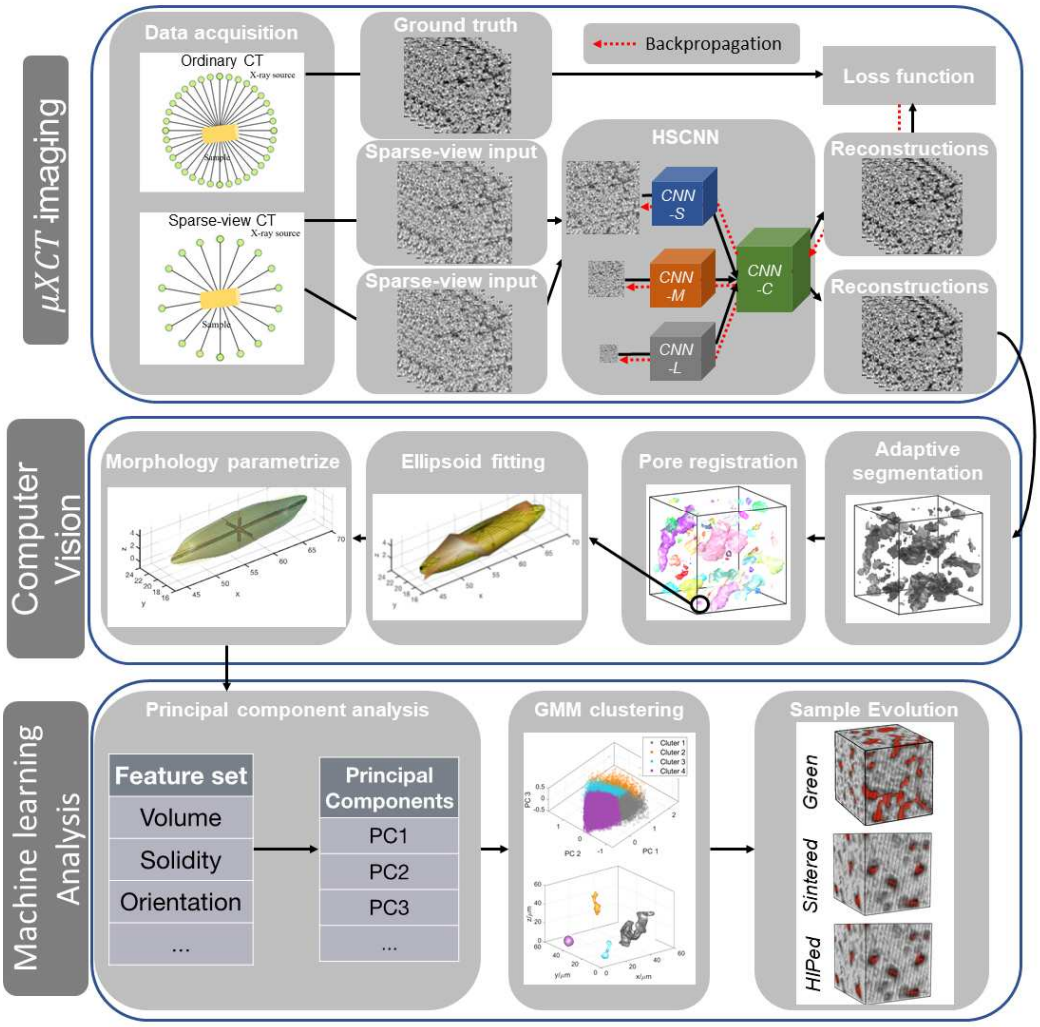

Figure 1. Framework of the 3D inspection pipeline for pore evolution in post-processing of additive manufacturing, including three major components of 1) μXCT data acquisition, 2) 3D morphological and statistical analysis, and 3) machine learning analysis. GMM stands for Gaussian mixture model.

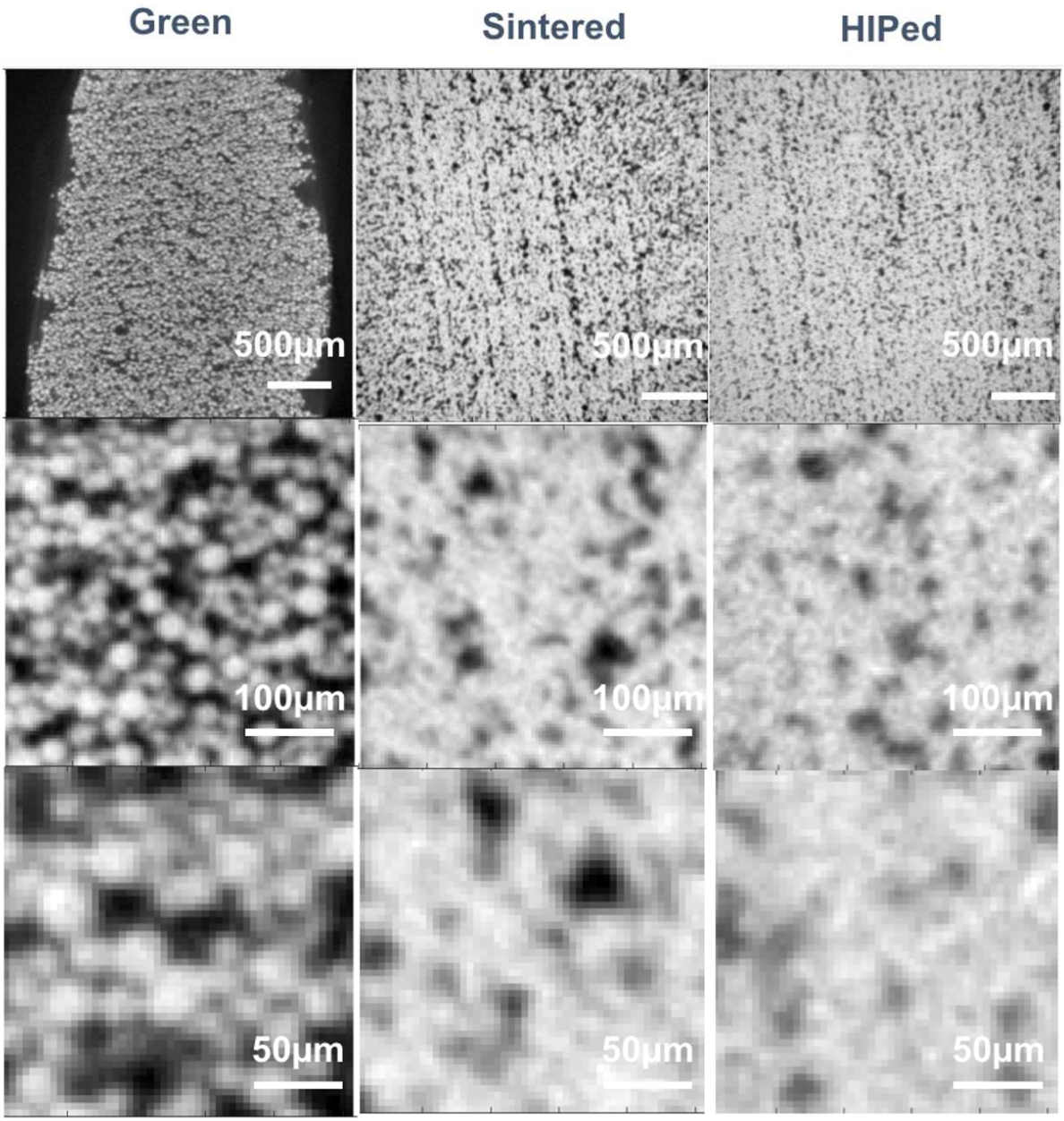

Figure 2. Results of the µXCT imaging in 2D representation. Slices of cropped region with different magnification are shown for the green, sintered, and HIPed samples, respectively.

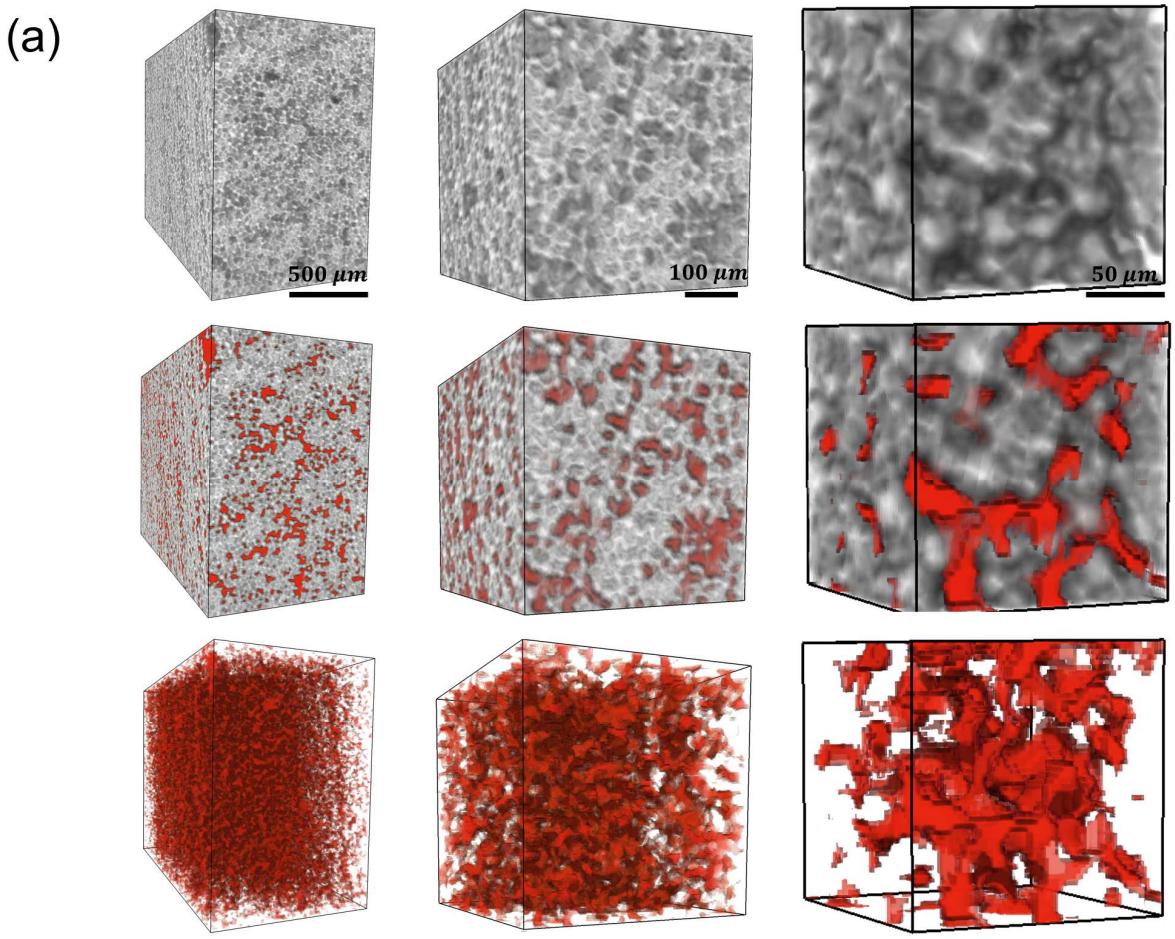

Figure 3. Results of the µXCT and pore extraction. 3D volumetric renderings are shown at three different scales for (1st row) raw µXCT reconstruction, (2nd row) raw reconstruction with embedded pores in red and (3rd row) extracted pores only, respectively. (a) The green sample.

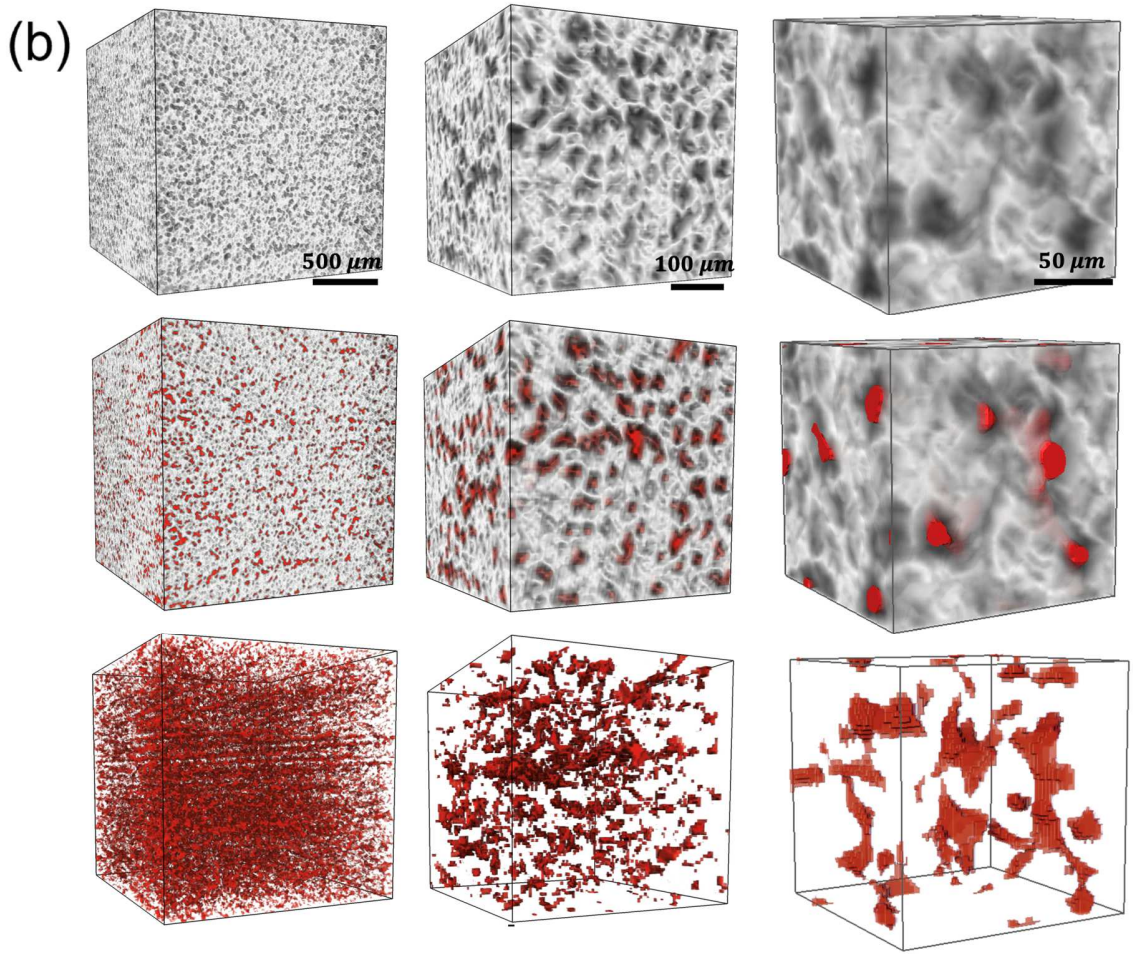

(b) The sintered sample.

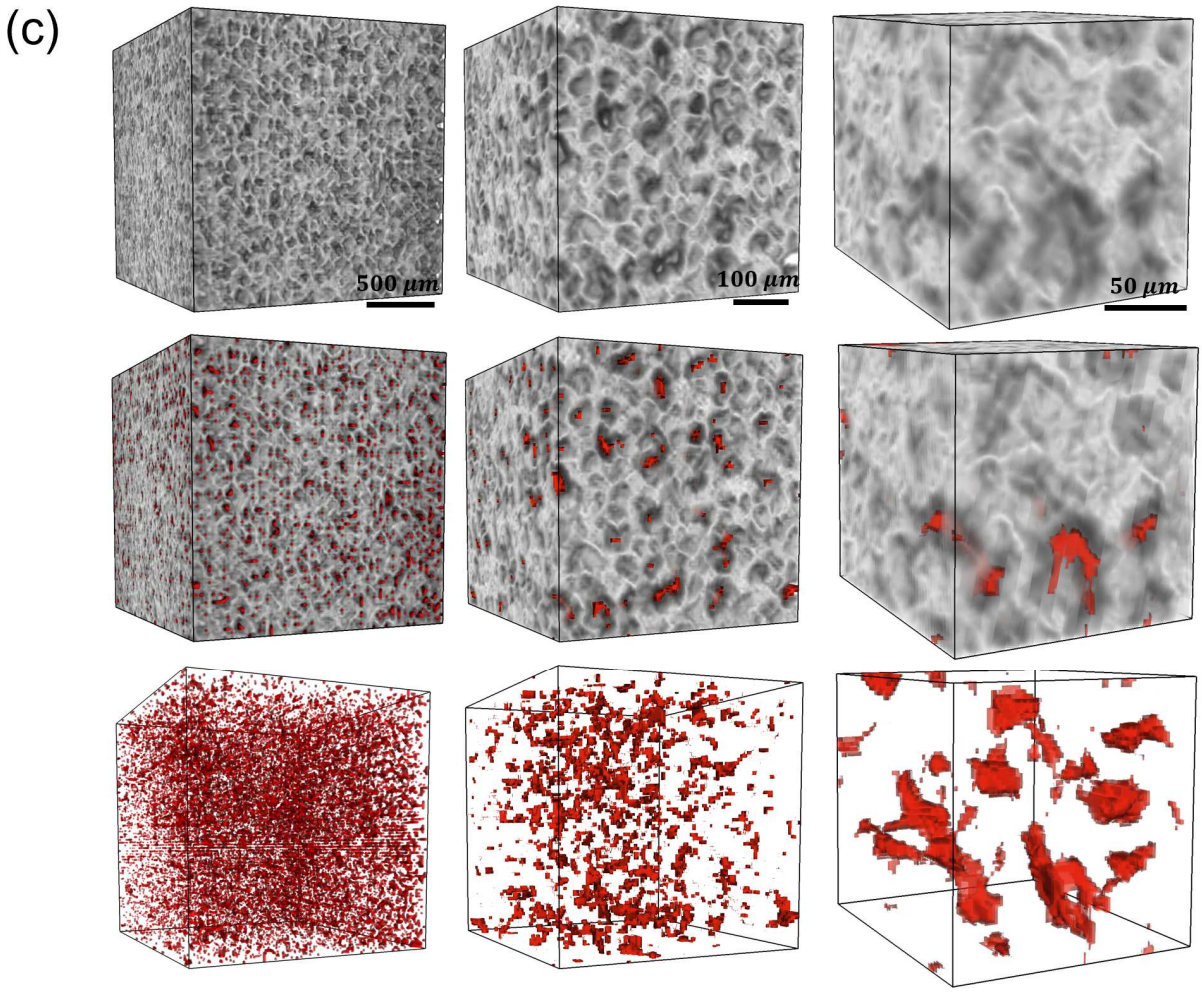

(c) The HIPed sample.

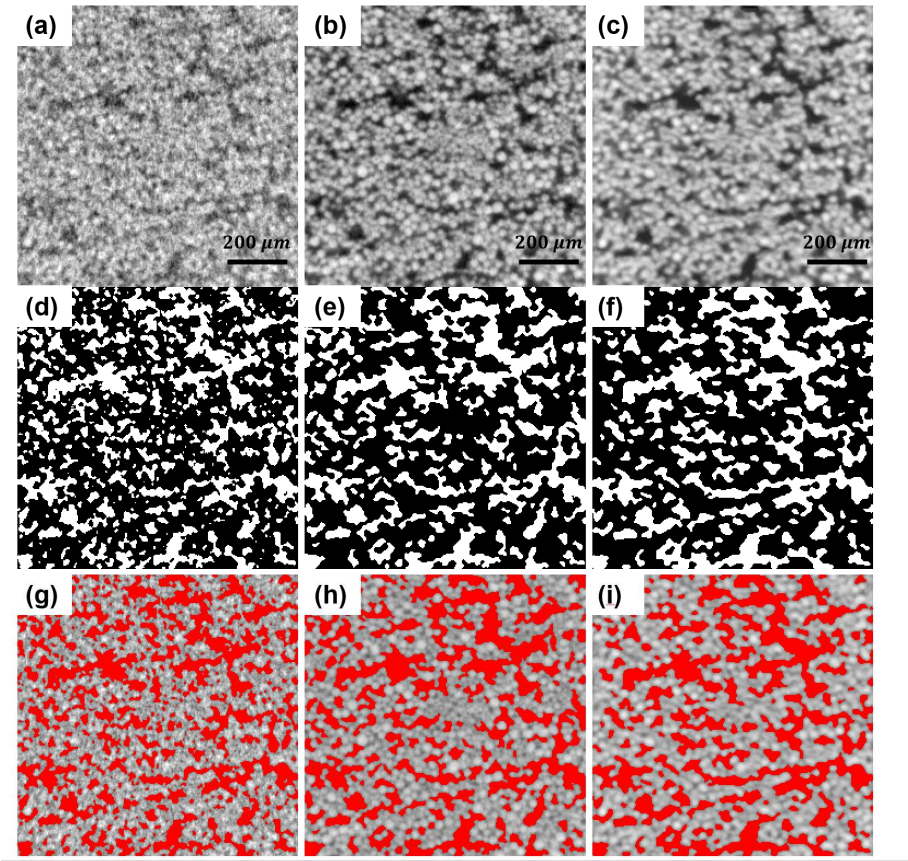

Figure 4. Fast tomography reconstruction for the green sample. The left column figures ((a), (d), (g)) represent the sparse-view reconstruction results. The middle column figures ((b), (e), (h)) represent the ground truth from the full-scan reconstruction. The right column figures ((c), (f), (i)) represent the high-fidelity reconstruction through deep learning based on sparse-view reconstruction. The 1st, 2nd, and 3rd row show the original gray-scale reconstruction results, the corresponding segmentation results, and the corresponding pore extraction results, respectively.

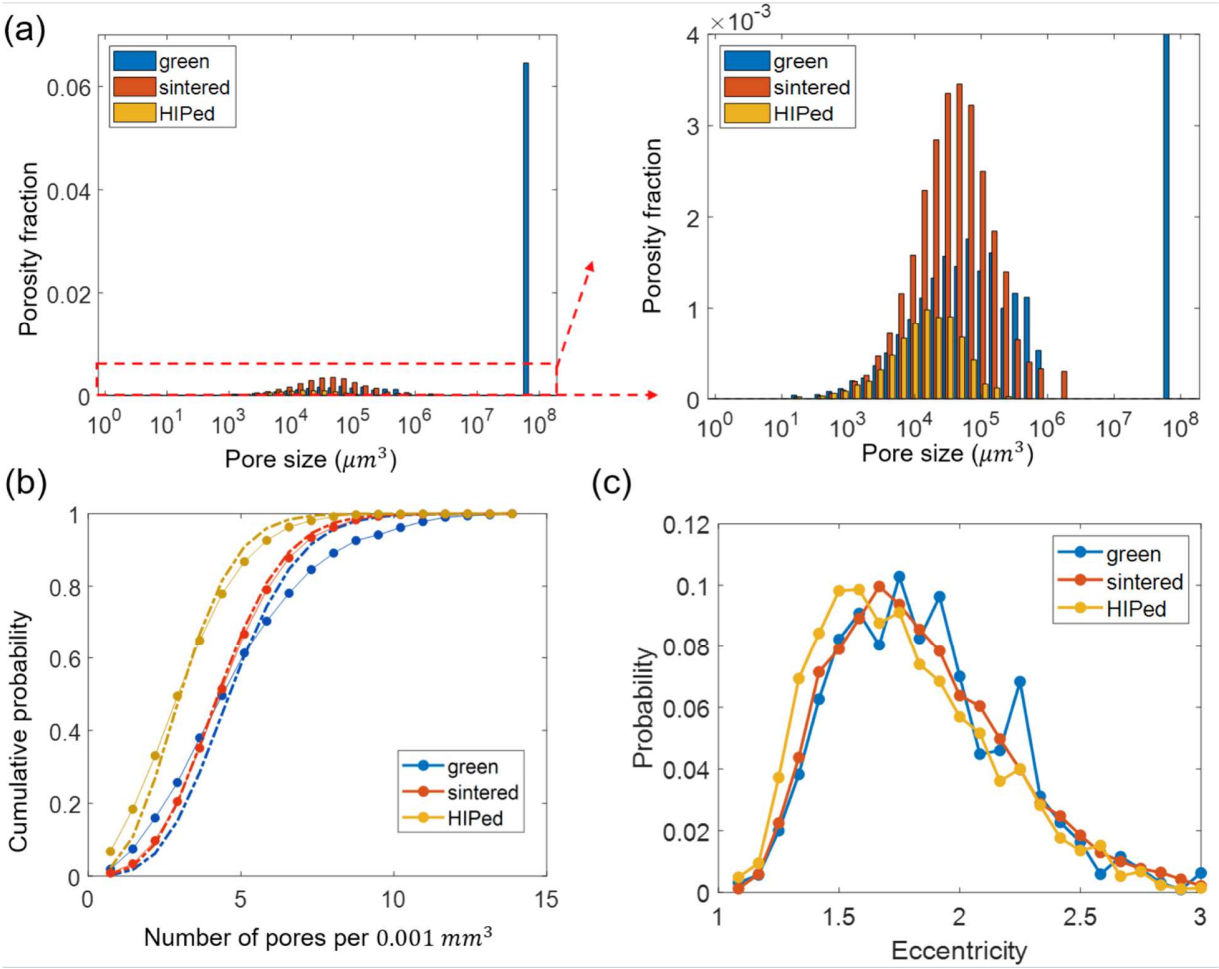

Figure 5. Statistical analysis results for the pores in the green, sintered and HIPed samples respectively. (a) The porosity fraction distribution of pore size (represented by the pore volume). Note that the singularity peak on the right represents a large interconnected pore in the green sample. Also shown is a 'zoom-in' view of the porosity fraction distribution without the singularity peak. (b) Cumulative probability distribution of the pore number density. (c) Probability distribution of eccentricity.

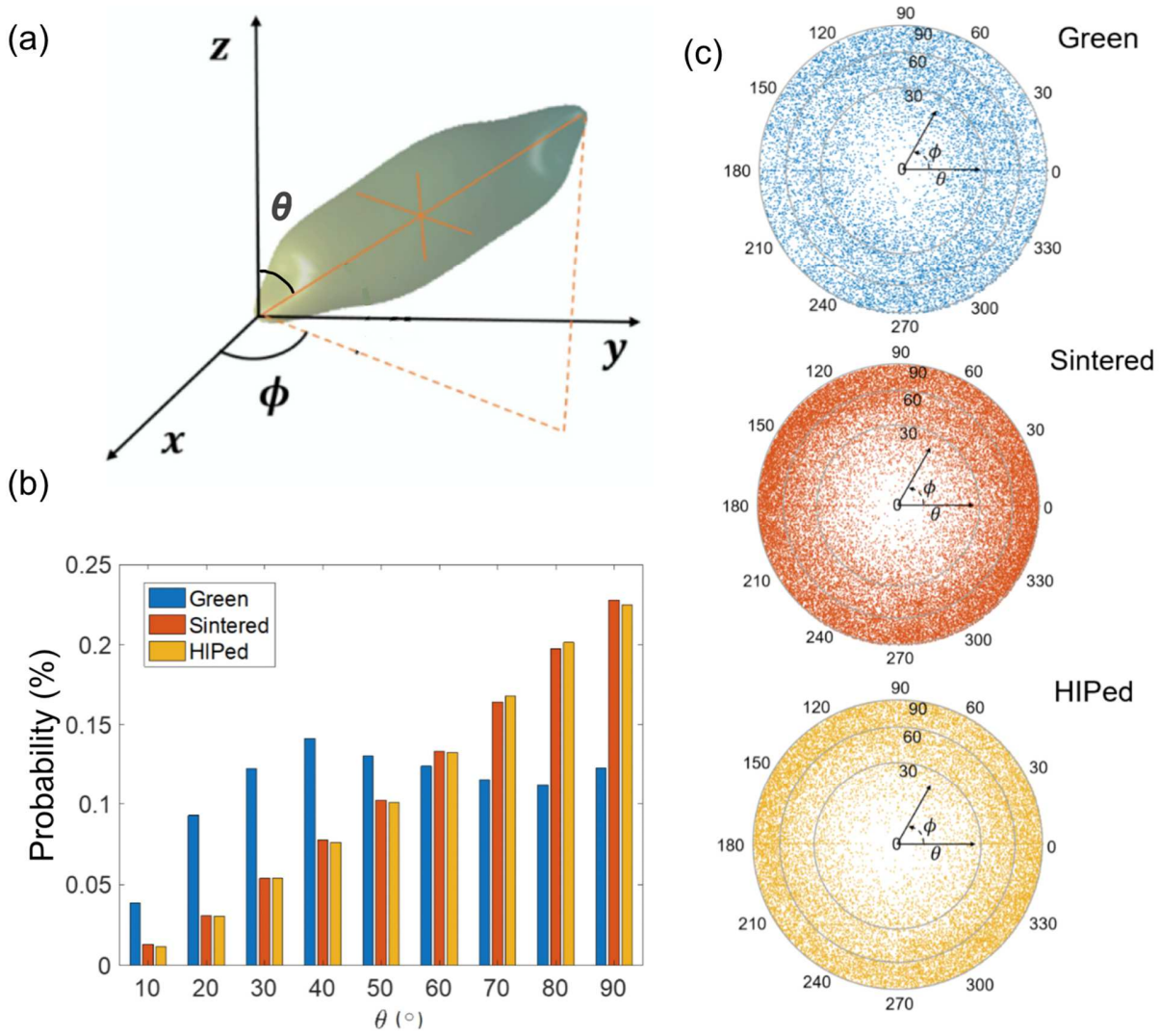

Figure 6. Orientation distribution of the pores in the three samples. (a) Definition of the azimuth angle ϕ and the altitude angle θ. (b) Probability distribution of the altitude angle θ. (c) Orientation distribution in polar plots for the green, sintered and HIPed samples, respectively. Preference of the altitude angle towards 90 degrees in sintered and HIPed samples can be observed from the peak position in (b), as well as from the concentration of data points in the outer rim in (c).

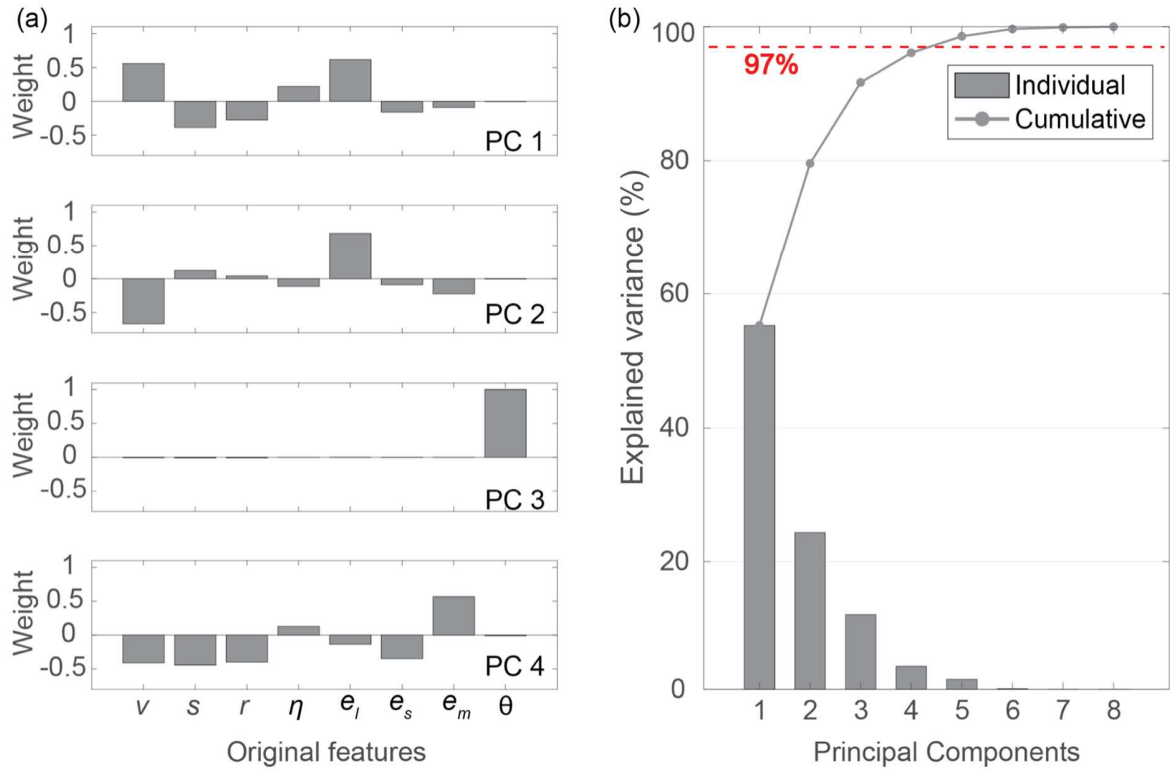

Figure 7. (a) The first four principal components shown as weight of the linear combinations of the eight morphology parameters (as summarized in Table 3). (b) Explanation level of each principal component. The first four PCs explain around 97% variance in the original morphological data.

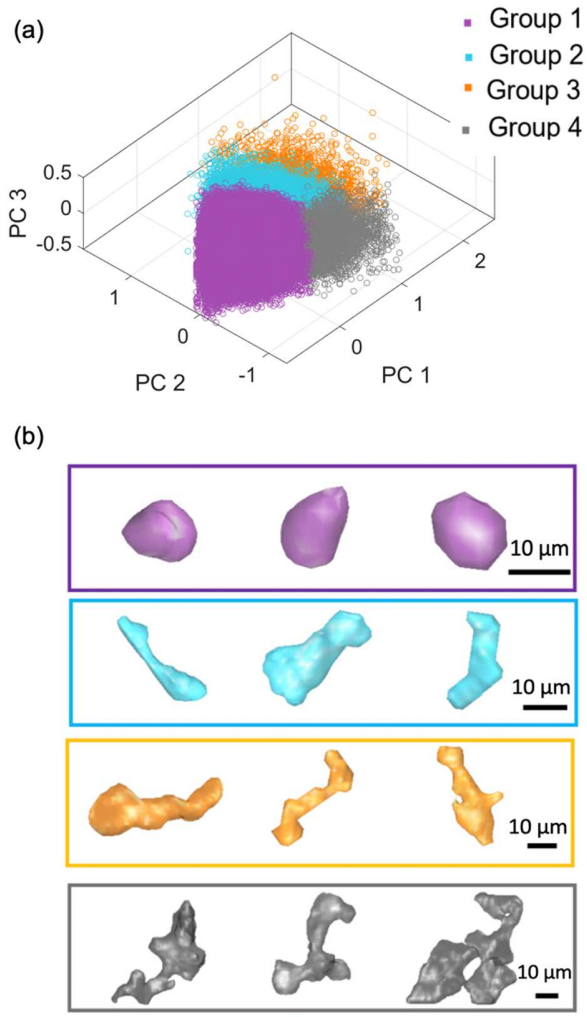

Figure 8. Clustering analysis results. (a) Four identified pore groups shown in the three-dimensional PC domain. (b) Examples of representative pores in each group.

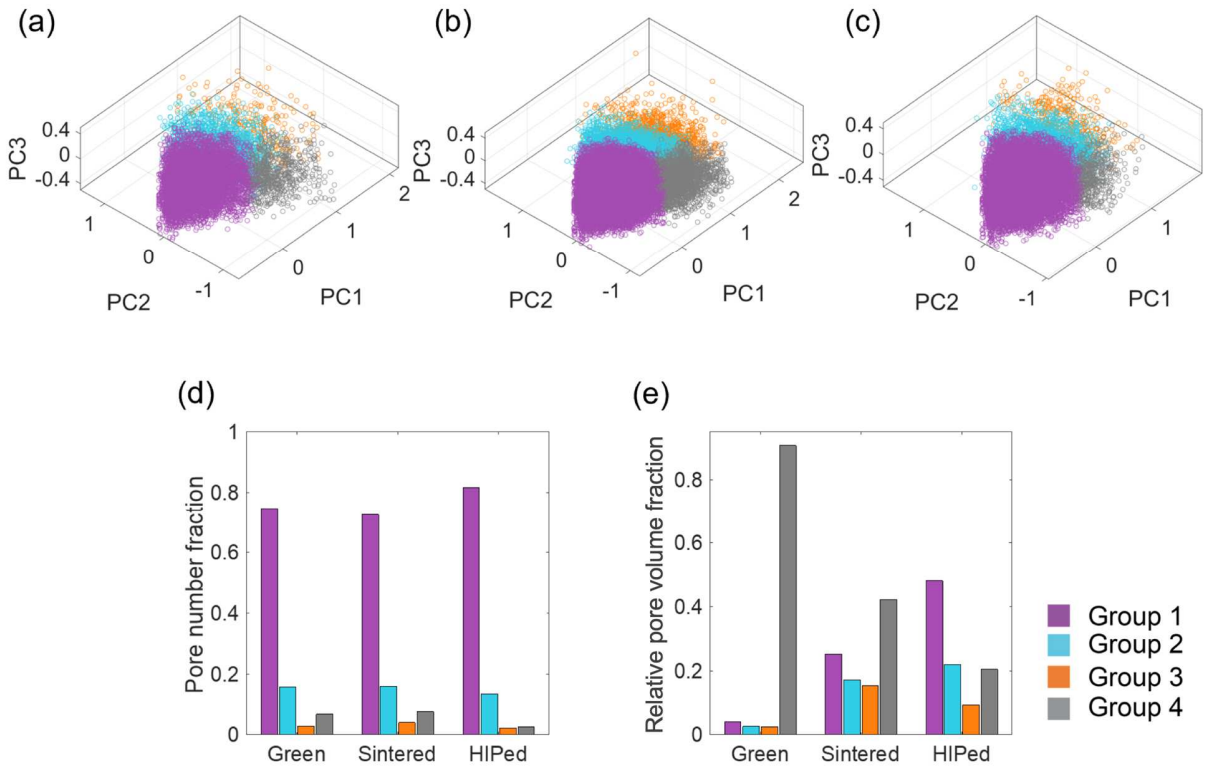

Figure 9. Evolution of pore morphology based on clustering analysis for the (a) green, (b) sintered, and (c) HIPed samples, respectively. Quantitative evolution of (d) pore number fraction and (e) relative volume fraction for the four pore groups.

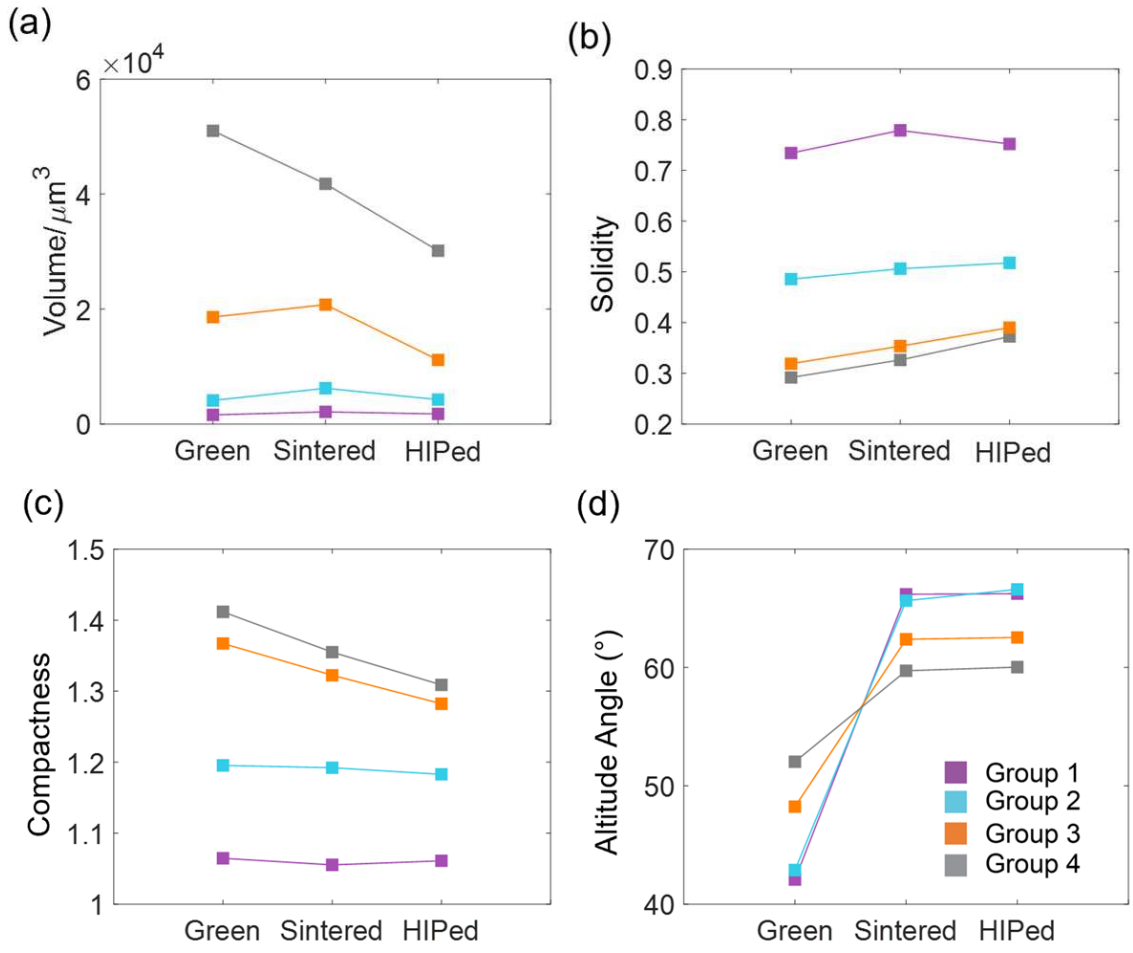

Figure 10. Evolution of the morphological parameters within each pore group for the green, sintered, and HIPed samples, plotted by the averaging value within each group for (a) the volume, (b) the solidity, (c) the compactness, and (d) the altitude angle.

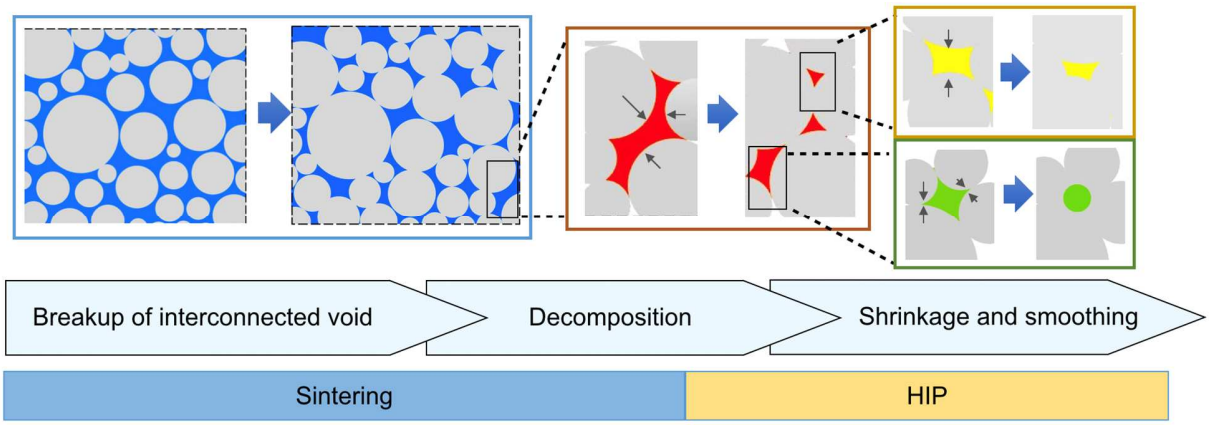

Figure 11. Pore morphology evolution mechanisms during the post-processing of sintering and HIP in binder jetting. The blue, red, yellow and green colors represent the four pore evolution patterns of 1) pore segmentation due to densification of loose particles, 2) decomposition of interconnected pore due to necking, 3) pore shrinkage and 4) pore smoothing.

References

1. Bai, Y. and C.B. Williams, *An exploration of binder jetting of copper.* Rapid Prototyping Journal, 2015.
2. Ma, P., et al., *Influence of annealing on mechanical properties of Al-20Si processed by selective laser melting.* Metals, 2014. **4**(1): p. 28-36.
3. Prashanth, K.G., et al., *Microstructure and mechanical properties of Al–12Si produced by selective laser melting: Effect of heat treatment.* Materials Science and Engineering: A, 2014. **590**: p. 153-160.
4. Prashanth, K., et al., *Production of high strength Al85Nd8Ni5Co2 alloy by selective laser melting.* Additive Manufacturing, 2015. **6**: p. 1-5.
5. Mostafaei, A., et al., *Microstructural evolution and mechanical properties of differently heat-treated binder jet printed samples from gas-and water-atomized alloy 625 powders.* Acta Materialia, 2017. **124**: p. 280-289.
6. Tan, X., et al., *Graded microstructure and mechanical properties of additive manufactured Ti–6Al–4V via electron beam melting.* Acta Materialia, 2015. **97**: p. 1-16.
7. Griffiths, R.J., et al., *A Perspective on Solid-State Additive Manufacturing of Aluminum Matrix Composites Using MELD.* Journal of Materials Engineering and Performance, 2019. **28**(2): p. 648-656.
8. Hang, Z.Y., et al., *Non-beam-based metal additive manufacturing enabled by additive friction stir deposition.* Scripta Materialia, 2018. **153**: p. 122-130.
9. Griffiths, R.J., et al., *Additive Friction Stir-Enabled Solid-State Additive Manufacturing for the Repair of 7075 Aluminum Alloy.* Applied Sciences, 2019. **9**(17): p. 3486.
10. Mostafaei, A., et al., *Powder bed binder jet printed alloy 625: Densification, microstructure and mechanical properties.* Materials & Design, 2016. **108**: p. 126-135.
11. Kumar, A.Y., et al., *Impacts of process-induced porosity on material properties of copper made by binder jetting additive manufacturing.* Materials & Design, 2019. **182**: p. 108001.
12. Hojjatzadeh, S.M.H., et al., *Pore elimination mechanisms during 3D printing of metals.* Nature communications, 2019. **10**(1): p. 1-8.
13. Everton, S.K., et al., *Review of in-situ process monitoring and in-situ metrology for metal additive manufacturing.* Materials & Design, 2016. **95**: p. 431-445.
14. Seifi, M., et al., *Progress towards metal additive manufacturing standardization to support qualification and certification.* Jom, 2017. **69**(3): p. 439-455.
15. Lu, Q.Y. and C.H. Wong, *Additive manufacturing process monitoring and control by non-destructive testing techniques: challenges and in-process monitoring.* Virtual and physical prototyping, 2018. **13**(2): p. 39-48.
16. Ziel, R., A. Haus, and A. Tulke, *Quantification of the pore size distribution (porosity profiles) in microfiltration membranes by SEM, TEM and computer image analysis.* Journal of membrane science, 2008. **323**(2): p. 241-246.
17. Ioannidis, M., M. Kwiecien, and I. Chatzis, *Statistical analysis of the porous microstructure as a method for estimating reservoir permeability.* Journal of petroleum science and engineering, 1996. **16**(4): p. 251-261.
18. Ehrlich, R., et al., *Petrography and reservoir physics I: Objective classification of reservoir porosity (1).* AAPG bulletin, 1991. **75**(10): p. 1547-1562.
19. Siddiq, A. and T. El Sayed, *Ultrasonic-assisted manufacturing processes: variational model and numerical simulations.* Ultrasonics, 2012. **52**(4): p. 521-529.
20. Cerniglia, D. and N. Montinaro, *Defect detection in additively manufactured components: Laser ultrasound and laser thermography comparison.* Procedia Structural Integrity, 2018. **8**: p. 154-162.
21. du Plessis, A. and S.G. le Roux, *Standardized X-ray tomography testing of additively manufactured parts: A round robin test.* Additive Manufacturing, 2018. **24**: p. 125-136.

22. Du Plessis, A., et al., *X-ray microcomputed tomography in additive manufacturing: a review of the current technology and applications.* 3D Printing and Additive Manufacturing, 2018. **5**(3): p. 227-247.
23. Wits, W.W., et al., *Porosity testing methods for the quality assessment of selective laser melted parts.* CIRP annals, 2016. **65**(1): p. 201-204.
24. King, W.E., et al., *Observation of keyhole-mode laser melting in laser powder-bed fusion additive manufacturing.* Journal of Materials Processing Technology, 2014. **214**(12): p. 2915-2925.
25. Aboulkhair, N.T., et al., *Reducing porosity in AlSi10Mg parts processed by selective laser melting.* Additive Manufacturing, 2014. **1**: p. 77-86.
26. Flodberg, G., H. Pettersson, and L. Yang, *Pore analysis and mechanical performance of selective laser sintered objects.* Additive Manufacturing, 2018. **24**: p. 307-315.
27. Cai, X., et al., *Measurement and characterization of porosity in aluminium selective laser melting parts using X-ray CT.* Virtual and Physical Prototyping, 2015. **10**(4): p. 195-206.
28. Landron, C., et al., *Validation of void growth models using X-ray microtomography characterization of damage in dual phase steels.* Acta Materialia, 2011. **59**(20): p. 7564-7573.
29. Mosavi, A., T. Rabczuk, and A.R. Varkonyi-Koczy. *Reviewing the novel machine learning tools for materials design*. in *International Conference on Global Research and Education*. 2017. Springer.
30. Dimiduk, D.M., E.A. Holm, and S.R. Niezgoda, *Perspectives on the impact of machine learning, deep learning, and artificial intelligence on materials, processes, and structures engineering.* Integrating Materials and Manufacturing Innovation, 2018. **7**(3): p. 157-172.
31. DeCost, B.L., et al., *Computer vision and machine learning for autonomous characterization of am powder feedstocks.* Jom, 2017. **69**(3): p. 456-465.
32. Cha, Y.J., W. Choi, and O. Büyüköztürk, *Deep learning-based crack damage detection using convolutional neural networks.* Computer-Aided Civil and Infrastructure Engineering, 2017. **32**(5): p. 361-378.
33. Schmidhuber, J., *Deep learning in neural networks: An overview.* Neural networks, 2015. **61**: p. 85-117.
34. Slotwinski, J.A., E.J. Garboczi, and K.M. Hebenstreit, *Porosity measurements and analysis for metal additive manufacturing process control.* Journal of research of the National Institute of Standards and Technology, 2014. **119**: p. 494.
35. Cunningham, R., et al., *Synchrotron-based X-ray microtomography characterization of the effect of processing variables on porosity formation in laser power-bed additive manufacturing of Ti-6Al-4V.* Jom, 2017. **69**(3): p. 479-484.
36. Du Plessis, A., et al., *Application of microCT to the non-destructive testing of an additive manufactured titanium component.* Case Studies in Nondestructive Testing and Evaluation, 2015. **4**: p. 1-7.
37. Kachanov, M., *Elastic solids with many cracks and related problems*, in *Advances in applied mechanics*. 1993, Elsevier. p. 259-445.
38. Kachanov, M., I. Tsukrov, and B. Shafiro, *Effective moduli of solids with cavities of various shapes.* 1994.
39. Romano, S., et al., *Qualification of AM parts: Extreme value statistics applied to tomographic measurements.* Materials & Design, 2017. **131**: p. 32-48.
40. Romano, S., S. Beretta, and M. Cova, *Quality control of cast iron: extreme value statistics applied to CT measurements.* Procedia Structural Integrity, 2017. **7**: p. 275-282.
41. Slotwinski, J.A., et al., *Characterization of metal powders used for additive manufacturing.* Journal of research of the National Institute of Standards and Technology, 2014. **119**: p. 460.
42. Wu, Z., et al. *Hierarchical convolutional network for sparse-view X-ray CT reconstruction.* in *Computational Imaging IV*. 2019. International Society for Optics and Photonics.
43. Han, Y. and J.C. Ye, *Framing U-Net via deep convolutional framelets: Application to sparse-view CT.* IEEE transactions on medical imaging, 2018. **37**(6): p. 1418-1429.

44. Jin, K.H., et al., *Deep convolutional neural network for inverse problems in imaging.* IEEE Transactions on Image Processing, 2017. **26**(9): p. 4509-4522.
45. Wu, Z., et al., *Robust X-ray Sparse-view Phase Tomography via Hierarchical Synthesis Convolutional Neural Networks.* arXiv preprint arXiv:1901.10644, 2019.
46. Veenman, C.J., M.J.T. Reinders, and E. Backer, *A maximum variance cluster algorithm.* IEEE Transactions on pattern analysis and machine intelligence, 2002. **24**(9): p. 1273-1280.
47. Vermunt, J.K. and J. Magidson, *Latent class cluster analysis.* Applied latent class analysis, 2002. **11**: p. 89-106.
48. Kanungo, T., et al., *An efficient k-means clustering algorithm: Analysis and implementation.* IEEE transactions on pattern analysis and machine intelligence, 2002. **24**(7): p. 881-892.
49. Jolliffe, I.T. and J. Cadima, *Principal component analysis: a review and recent developments.* Philosophical Transactions of the Royal Society A: Mathematical, Physical and Engineering Sciences, 2016. **374**(2065): p. 20150202.
50. Xu, D. and Y. Tian, *A comprehensive survey of clustering algorithms.* Annals of Data Science, 2015. **2**(2): p. 165-193.
51. Lykov, P., E. Safonov, and A. Akhmedianov. *Selective laser melting of copper*. in *Materials Science Forum*. 2016. Trans Tech Publ.
52. Kastner, J. and C. Heinzl, *X-ray computed tomography for non-destructive testing and materials characterization*, in *Integrated Imaging and Vision Techniques for Industrial Inspection*. 2015, Springer. p. 227-250.
53. Wu, Z., et al. *Feature-based sparse angle tomography reconstruction for dynamic characterization of bio-cellular materials*. in *Computational Imaging III*. 2018. International Society for Optics and Photonics.
54. Thompson, A., et al., *Effects of magnification and sampling resolution in X-ray computed tomography for the measurement of additively manufactured metal surfaces.* Precision Engineering, 2018. **53**: p. 54-64.
55. Xie, S., et al., *Artifact removal using improved GoogLeNet for sparse-view CT reconstruction.* Scientific reports, 2018. **8**(1): p. 1-9.
56. Pelt, D.M. and J.A. Sethian, *A mixed-scale dense convolutional neural network for image analysis.* Proceedings of the National Academy of Sciences, 2018. **115**(2): p. 254-259.
57. Pelt, D.M., K.J. Batenburg, and J.A. Sethian, *Improving tomographic reconstruction from limited data using mixed-scale dense convolutional neural networks.* Journal of Imaging, 2018. **4**(11): p. 128.
58. Wu, Z., X. Wu, and Y. Zhu, *Structured illumination-based phase retrieval via Generative Adversarial Network*. SPIE BiOS. Vol. 11249. 2020: SPIE.
59. Yang, T., et al., *Quantitative 3D structural analysis of the cellular microstructure of sea urchin spines (I): Methodology.* Acta Biomaterialia, 2020.
60. Chen, H., et al., *Quantitative 3D structural analysis of the cellular microstructure of sea urchin spines (II): Large-volume structural analysis.* Acta Biomaterialia, 2020.
61. Lehmann, G. and D. Legland, *Efficient N-dimensional surface estimation using Crofton formula and run-length encoding.* Efficient N-Dimensional surface estimation using Crofton formula and run-length encoding, Kitware INC (2012), 2012.
62. Vrieze, S.I., *Model selection and psychological theory: a discussion of the differences between the Akaike information criterion (AIC) and the Bayesian information criterion (BIC).* Psychological methods, 2012. **17**(2): p. 228.
63. Burnham, K.P. and D.R. Anderson, *Multimodel inference: understanding AIC and BIC in model selection.* Sociological methods & research, 2004. **33**(2): p. 261-304.
64. Kumar, A., et al., *Effects of hot isostatic pressing on copper parts fabricated via binder jetting.* Procedia Manufacturing, 2017. **10**: p. 935-944.
65. Kumar, A.Y., et al., *The effects of Hot Isostatic Pressing on parts fabricated by binder jetting additive manufacturing.* Additive Manufacturing, 2018. **24**: p. 115-124.

66. Gonzalez, J., et al., *Characterization of ceramic components fabricated using binder jetting additive manufacturing technology.* Ceramics International, 2016. **42**(9): p. 10559-10564.
67. Bocanegra-Bernal, M., *Hot isostatic pressing (HIP) technology and its applications to metals and ceramics.* Journal of Materials Science, 2004. **39**(21): p. 6399-6420.
68. Mostafaei, A., et al., *Effect of powder size distribution on densification and microstructural evolution of binder-jet 3D-printed alloy 625.* Materials & Design, 2019. **162**: p. 375-383.
69. Shanker, M., M.Y. Hu, and M.S. Hung, *Effect of data standardization on neural network training.* Omega, 1996. **24**(4): p. 385-397.
70. Cramer, C.L., et al., *Infiltration studies of additive manufacture of WC with Co using binder jetting and pressureless melt method.* Additive Manufacturing, 2019. **28**: p. 333-343.
71. Mostafaei, A., et al., *Characterizing surface finish and fatigue behavior in binder-jet 3D-printed nickel-based superalloy 625.* Additive Manufacturing, 2018. **24**: p. 200-209.
72. Hermanek, P., F. Zanini, and S. Carmignato, *Traceable porosity measurements in industrial components using X-ray computed tomography.* Journal of Manufacturing Science and Engineering, 2019. **141**(5).